Inorganic Chemistry
Article
pubs.acs.org/IC

Hierarchical MnO_2/SnO_2 Heterostructures for a Novel Free-Standing Ternary Thermite Membrane

Yong Yang, Zhi-Cheng Zhang, Peng-Peng Wang, Jing-Chao Zhang, Farhat Nosheen, Jing Zhuang, and Xun Wang*

Department of Chemistry, Tsinghua University, Beijing 100084, P. R. China

Supporting Information

ABSTRACT: We report the synthesis of a novel hierarchical MnO_2/SnO_2 heterostructures via a hydrothermal method. Secondary SnO_2 nanostructure grows epitaxially on the surface of MnO_2 backbones without any surfactant, which relies on the minimization of surface energy and interfacial lattice mismatch. Detailed investigations reveal that the cover density and morphology of the SnO_2 nanostructure can be tailored by changing the experimental parameter. Moreover, we demonstrate a bottom-up method to produce energetic nanocomposites by assembling nanoaluminum (n-Al) and MnO_2/SnO_2 hierarchical nanostructures into a free-standing MnO_2/SnO_2/n-Al ternary thermite membrane. This assembled approach can significantly reduce diffusion distances and increase their intimacy between the components. Different thermite mixtures were investigated to evaluate the corresponding activation energies using DSC techniques. The energy performance of the ternary thermite membrane can be manipulated through different components of the MnO_2/SnO_2 heterostructures. Overall, our work may open a new route for new energetic materials.

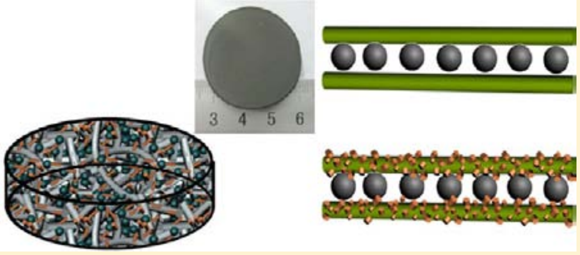

INTRODUCTION

Hierarchical nanostructures have attracted intensive attention because of the exciting physical and chemical properties resulting from their diverse functionalities.[1−3] Various physical and chemical methods, such as physical vapor deposition and chemical bath deposition, have been reported to synthesize a number of heterostructures.[4] Among them, one-dimensional (1D) hierarchical heterostructures appear to be the most promising building blocks for further electronic devices and other advanced functional systems.[5−7] Recently, considerable progress has been made in fabricating different types of 1D hierarchical heterostructures. Nevertheless, the synthesis of various components as the building blocks of hierarchical nanostructures is still a great challenge. It is necessary to further explore new one-dimensional heterostructures with different components to expand their application.

Metastable intermolecular composites (MICs), as a new class of energetic materials, are mainly composed of metal oxides and fuel nanoparticles based on the general oxidation−reduction reaction shown in eq 1.[8]

$$M_xO_y + Al \rightarrow M + Al_2O_3 \qquad (1)$$

Aluminum is usually chosen as the fuel component owing to the high heat of formation of alumina. These nanocomposites have potential in military applications,[9] which generally exhibit extremely high adiabatic flame temperatures and energy release compared to their bulk counterparts because of the much larger surface areas and lesser mass transfer distance. Over the past decade, investigations focused on the synthesis of nanoscale fuel and oxidizers and how to improve the intimacy of the binary component.[10−14] Thermite composites composed of oppositely charging n-Al and Fe_2O_3 have been reported based on electrostatic self-assembly.[15] n-Al/CuO_x based nano-energetic materials (nEMs) have been made by integrating Al into CuO nanowire though thermal evaporation.[16] More recently, Severac et al. showed that a high-energy n-Al/CuO composite was obtained by DNA-directed assembly. In that study, DNA was used as a bridge to realize assembly between Al and CuO.[17] Few reports pay attention to the synthesis of ternary thermite. In addition, thermite composites obtained using the conventional mixing method were difficult to integrate into devices owing to their powder form. These shortages greatly limit their application.[18,19] It is necessary to prepare novel thermite composites with tunable properties to meet various demands.

Different metal oxide/SnO_2 heterostructures were reported using various approaches.[20−24] In this paper, we synthesize the MnO_2/SnO_2 hierarchical heterostructures using a simple hydrothermal method using $Sn(OH)_6^{2-}$ as the precursor without any surfactant. Detailed investigations revealed that the density and morphology of the SnO_2 nanostructure can be tailored by changing the precursor concentration and reaction temperature. The secondary SnO_2 nanostructures are epitaxially grown on the surface of the MnO_2 nanowire substrates without any symmetric model, which results from the minimization of surface energy and interfacial lattice mismatches. Moreover, a free-standing MnO_2/SnO_2/n-Al ternary thermite membrane

Received: April 29, 2013
Published: August 1, 2013

was prepared through a water-based processing method. This bottom-up method can not only decrease the diffusion distance but also increase the intimate contact between the components. This novel membrane-based nanothermite will be easily integrated into a device due to its processable and portable property. Compared with other thermite composites, the secondary SnO_2 nanostructure as an inert component separates the fuel and oxidizer. In addition, the total energy released and the behavior of the thermite reaction can be tuned via different components of the MnO_2/SnO_2 heterostructures. This effect enables us to moderate the thermite reaction for various applications by changing the oxidizer composition. This novel, free-standing thermite membrane is easily processable and portable. Advantages of this technique are the simplicity and having wide applicability to prepare many other thermite systems.

EXPERIMENTAL SECTION

Materials. All reagents are of analytical grade and used without further purification. Nanometer sized aluminum particles (n-Al) were purchased from Beijing Nachen S&T Ltd. Original aluminum nanoparticles were covered by an about several-nanometer-thick compact amorphous alumina passivation layer. As aluminum powder is aged, the thickness of this oxide layer increases. The average particle size distribution of aluminum powder is about 80 nm (Figure S1). Therefore, care should be taken in the storage and use of aluminum to avoid the oxidation of aluminum.

Synthesis of α-MnO_2 Nanowires. α-MnO_2 nanowires were synthesized using a hydrothermal method according to a previous paper.[25] Manganese sulfate monohydrate ($MnSO_4 \cdot H_2O$), ammonium persulfate ($(NH_4)_2S_2O_8$), and ammonium sulfate $(NH_4)_2SO_4$ in a molar ratio of 1:1:3 were added into 36 mL of distilled water under intense stirring to form a transparent solution and were transferred to a Teflon vessel held in a stainless steel vessel. The sealed vessel was placed in an oven and heated at 180 °C for 12 h. The product was washed with water several times to remove all soluble impurities.

Synthesis of MnO_2/SnO_2 Hierarchical Nanostructures. The SnO_2/MnO_2 hierarchical nanostructures were prepared using the hydrothermal method. Typically, 40 mg of MnO_2 nanowires was dispersed in deionized water by ultrasonic treatment for several minutes in a Teflon vessel. Then $SnCl_4 \cdot 4H_2O$ and NaOH were added into a MnO_2 suspension solution under magnetic stirring. Then, the resulting solution was transferred into a 40 mL Teflon-lined autoclave. The autoclave was sealed and heated at 200−220 °C for 3 h and then cooled to room temperature naturally. The products were collected, washed with ethanol and deionizer water, respectively, and then dried under a vacuum at 60 °C for 12 h.

Fabrication of Free-Standing MnO_2/SnO_2/n-Al Ternary Thermite Membrane. The free-standing $SnO_2/MnO_2/Al$ thermite membranes were fabricated using a simple filtration process. Briefly, SnO_2/MnO_2 hierarchical nanowires were dispersed in $NH_4H_2PO_4$ (0.1Wt %) aqueous water with ultrasonic treatment. n-Al was dispersed in isopropanol, forming a gray homogeneous suspension. n-Al was poured into a SnO_2/MnO_2 hierarchical nanowires solution keeping ultrasonic treatment. Finally, hybrid composites were transferred into a ceramic vacuum filter machine device. The free-standing SnO_2/MnO_2/n-Al thermite membrane can be easily detached from the substrate without any deterioration after vacuum suction filtration.

Characterization. The morphology and size of the nanostructures were determined by a LEO-1530 instrument coupled to an EDX-spectroscopy system at 10 kV, a HITACHI H-7650B transmission electron microscope (TEM) at 100 kV with an energy dispersive X-ray spectrometer (EDS) working at 20 kV, and a FEI Tecnai G2 F20 S-Twin high-resolution transmission electron microscope (HRTEM) at 200 kV. The samples were prepared by depositing and evaporating a droplet of the aqueous colloidal solution on a silicon pellet or on a carbon-coated copper grid. The crystal structure was analyzed with a Rigaku RU-200b X-ray powder diffractometer by using nickel-filtered Cu Ka radiation in the range 20−80° with a scan rate of 10°/min. Differential scanning calorimetry (DSC) measurements were performed on a SETARAM DSC 111G system under a nitrogen flow with a Supelco superclean gas-purifier oxygen trap over the temperature range from 300 to 1000 K and at a different heating rate. The samples were transferred and evaporated in an alumina crucible for thermal analysis.

RESULTS AND DISCUSSION

Structure Characterization and Mechanism Investigation. The microstructure and morphology of the heterostructures were initially observed as transmission electron microscope (TEM) images. As shown in Figure 1a,b and Figure S2, it is worth pointing out that secondary SnO_2 nanostructures were successfully grown on primary MnO_2 nanowire substrates without any symmetric features. Furthermore, element analysis mapping was carried out to investigate the distribution of heterostructures (see also Figure S3 in the Supporting Information). Energy dispersive spectroscopy (EDS) microanalysis was taken from MnO_2/SnO_2 heterostructured nanowires to investigate the formation (Figure 1c). It is clearly seen that the heterostructures consist of Sn, Mn, and O. XRD analysis (Figure 1d) further indicates that all the diffraction peaks of the heterostructures can be well indexed to the standard data of SnO_2 (JCPDS No. 41−1445) and MnO_2 (JCPDS No. 44−0141). No other impurity peaks are detected. Figure S4 displays the FT-IR spectrum of the as-synthesized MnO_2/SnO_2 heterostructured nanowires. The bands at 550 and 700 cm^{-1} can be attributed to the Mn−O and Sn−O vibrations, respectively. The bands at 3430 cm^{-1} and 1640 cm^{-1} correspond to the O−H vibrations of H_2O. These results confirm that the secondary SnO_2 heterostructures are well distributed on the surface of MnO_2 nanowires.

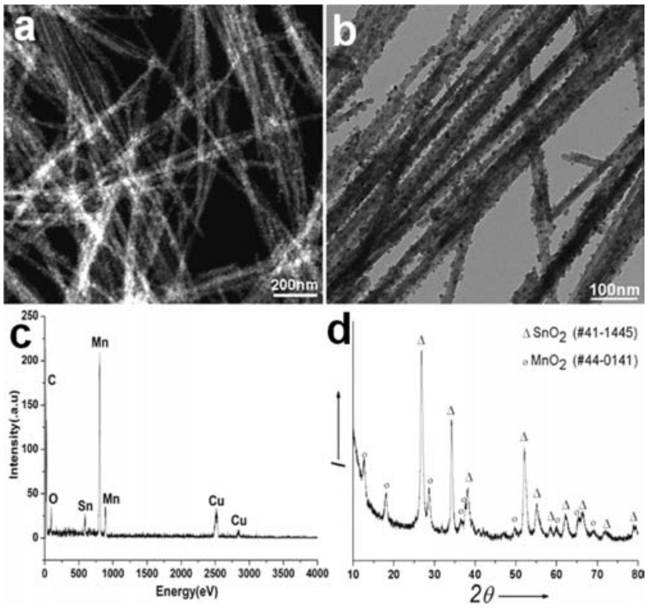

Figure 1. Materials characterization. (a,b) The high-angle annular dark-field scanning TEM (HAADF-STEM) and high-magnification TEM images of as-prepared MnO_2/SnO_2 hierarchical heterostructures. (c) EDS spectrum of MnO_2/SnO_2 hierarchical heterostructures. Presence of the Cu peaks in the spectrum comes from the copper grids used as a support in TEM observations. (d) XRD patterns of as-synthesized MnO_2/SnO_2 hierarchical heterostructures. Δ indicates the phase of SnO_2, and ○ indicates the phase of MnO_2.

To explore epitaxial growth of SnO_2 nanorods coupled with the MnO_2 nanowires, HRTEM analyses were conducted. It is clear to see that both the secondary structures and the backbone are single crystalline with clear lattice fringes in Figure 2a. Much attention should be focused on the interface between the MnO_2 backbone and SnO_2 nanostructures. Figure 2b−d show the main interface relation for hierarchical nanostructures. The border between SnO_2 nanostructures and MnO_2 nanowires is inconspicuous, indicating that secondary growth may occur between the interfaces. As shown in Figure 2b, the lattice spacing of 0.263 nm for the nanorods and 0.309 nm for the backbone nanowires correspond to the (101) plane of the SnO_2 and the (310) plane of MnO_2, respectively. Figure 2c shows the presence of crystalline MnO_2 and SnO_2 crystal lattice fringes observed in the region of the junction corresponding to the interplanar distances of 0.245 and 0.263 nm, which agrees well with the lattice spacing of the (400) plane of MnO_2 and the (101) plane of SnO_2 crystal, respectively. It was revealed that the SnO_2 nanoparticles on the surfaces of MnO_2 nanowires grow along the [101] direction and parallel to the (400) planes of MnO_2. From the HRTEM images shown in Figure 2d, besides the [101] growth direction, the [110] direction is also observed for secondary growth. It revealed that the SnO_2 nanorods were glued to the (110) surfaces of MnO_2 substrates with the interfacial orientation relationship as $(110)SnO_2//(110)MnO_2$. According to the previous report,[26] the sequence of surface energy per crystal face can be described as $(110) < (101) < (001)$ in the view of the crystal structure of SnO_2. Our results show secondary SnO_2 growth with specific growth directions including [101] or [110]. However, SnO_2 dendrite was obtained under similar conditions without a MnO_2 nanowire substrate (see Figure S5), which grew along [001] directions.[26]

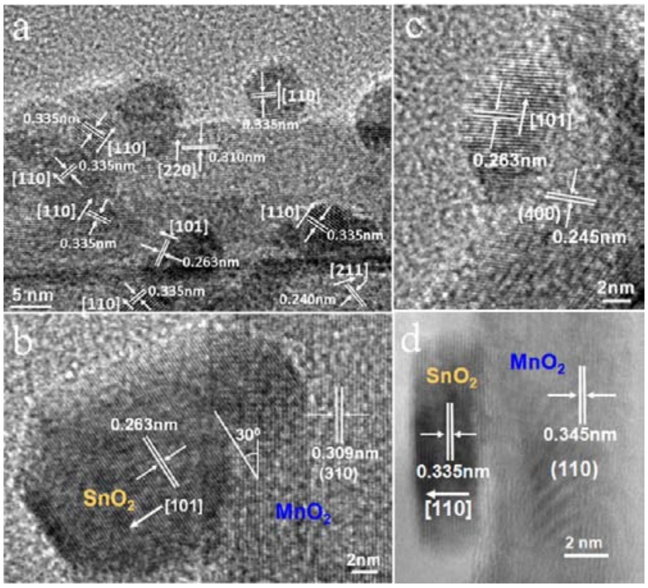

Figure 2. Structural characterization of the heterointerface. (a) High-resolution TEM showing the interface of SnO_2 nanostructure on the surface of MnO_2 nanowires. (b) SnO_2 grown along the [101] direction on the (310) surface of MnO_2 nanowires. (c) SnO_2 grown along the [101] direction on the (400) surface of MnO_2 nanowires. (d) SnO_2 grown along the [110] direction on the (110) surface of MnO_2 nanowires.

It is generally acknowledged that the formation of heterostructures results from the minimization of total system energy. In addition, interfacial lattice mismatch is of great importance for the epitaxial growth of heterogeneous structures. A smaller mismatch facilitates the formation of stable heterostructures. The heterostructures composed of MnO_2 and SnO_2 should be considered with a small lattice mismatch according to this theory. The lattice mismatch of different interfacial orientations was compared to investigate the growth direction of the SnO_2 nanostructure. As shown in Figure 2b, SnO_2 nanorods grew at an angle of 30° rather than the perpendicular growth with the normal of the MnO_2 (310) plane. This phenomenon can be explained by the minimization of lattice mismatches. The diagrams of the (310) surface of MnO_2 and (101) surface of SnO_2 are presented in Figure 3a and b, respectively. According to interfacial crystal lattice mismatch formula, vertical growth of SnO_2 along [101] on the MnO_2 (310) plane results in a large lattice mismatch of 14.8% $[(0.309 - 0.263)/0.309 \approx 14.8\%]$. In contrast, SnO_2 nanorods inclined at an angle of 30° to the normal of the MnO_2 (310) plane reduce the interfacial lattice mismatch to be 1.5% $[(0.309 - 0.304)/0.309 \approx 1.5\%]$. The schematic of the interface of the (010) SnO_2 plane of a SnO_2 nanorod and the (310) surface of MnO_2 nanowires are illustrated in Figure 3c. For $(110)SnO_2//(110)MnO_2$, the interfacial lattice mismatch can be calculated as 2.9% $[(0.345 - 0.335)/0.345 \approx 2.9\%]$. On the basis of the above analysis, different epitaxially grown orientations of the SnO_2 on the surface of MnO_2 nanowires substrates relies on the minimization of surface energy and interfacial lattice mismatches. It should be mentioned that most previous reports for SnO_2 hierarchical nanostructures feature similar 6-fold symmetry.[27−30] In our case, both MnO_2 and SnO_2 belong to the tetragonal structure. Secondary growth SnO_2 grows randomly on the surface of MnO_2 substrates. Therefore, the crystal structure of the substrate has a great influence on the SnO_2 secondary growth.

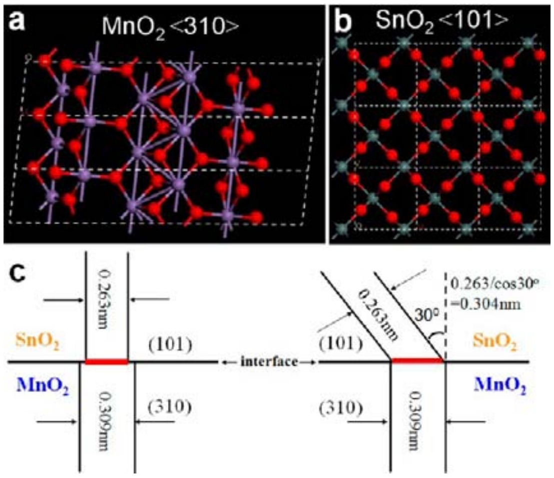

Figure 3. Crystal structure of MnO_2 and SnO_2. Diagram of (a) (310) surface of MnO_2, (b) (101) surface of SnO_2. Blue, dark green, and red balls represent manganese, tin, and oxygen, respectively. (c) Schematic of the interface of the $(101)_{SnO2}$ plane of SnO_2 nanorods and the $(310)_{MnO2}$ plane of MnO_2 nanowires. Red-line regions show the actual contact crystal planes.

The secondary SnO_2 nanostructures grown on MnO_2 nanowire substrates with different densities and shapes can be

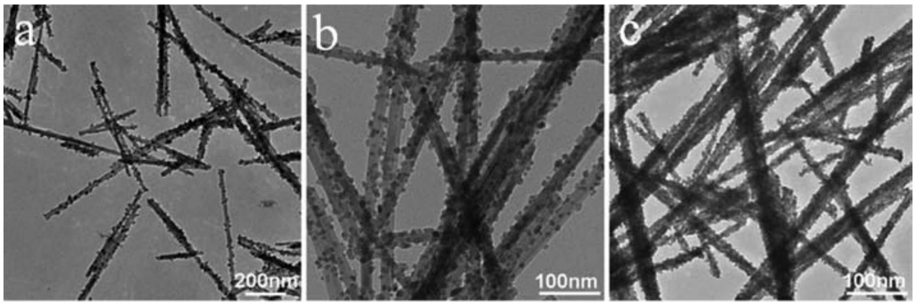

Figure 4. The different cover densities of SnO_2. TEM images of different densities of SnO_2 nanoparticles on the surface of MnO_2 nanowire substrates with increasing the precursor concentration (from left to right).

controlled by changing the experimental parameters such as precursor concentration and temperature. Figure 4 shows the TEM images of the as-obtained hierarchical heterostructures. It can be observed that the density of nanoparticles is dramatically increased when the amount of precursor changes from 0.13 mmol to 0.52 mmol. Figure 5a displays that the MnO_2 nanowires are of a relatively smooth surface with a length of several micrometers and a diameter of 20 nm. Figure 5b,c shows TEM images of the structures obtained under different growth conditions. For instance, with the increase of the temperature to 220 °C while other conditions keep constant, the morphology of secondary SnO_2 nanostructures grown on MnO_2 nanowires substrates changes to particles instead of nanorods. To clearly demonstrate the formation of hierarchical MnO_2/SnO_2 nanowires, the growth mechanism is given in Figure 5d. First, driven by the decrease of surface energy, SnO_2 nanoparticles randomly nucleated on the surfaces of the MnO_2 nanowires through the dehydration of $Sn(OH)_6{}^{2-}$. Then SnO_2 nanoparticles grew up on the surface of MnO_2 nanowires to form hierarchical heterostructures.

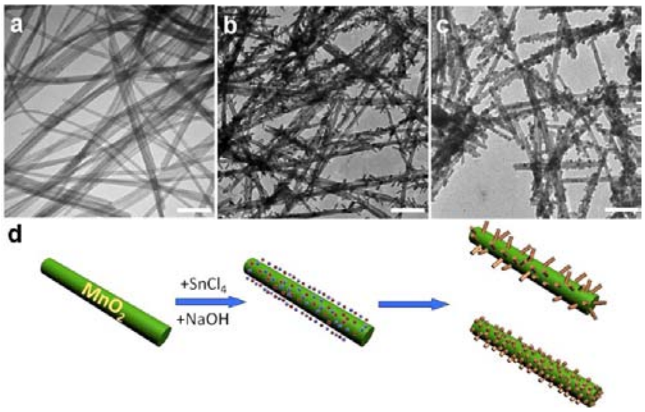

Figure 5. The construction of MnO_2/SnO_2 hierarchical nanostructures. (a) TEM image of MnO_2 nanowires. (b) The branches are individual SnO_2 nanorods under 200 °C. (c) The branches are individual SnO_2 nanoparticles under 220 °C. (d) Schematic of the formation process of hierarchical MnO_2/SnO_2 nanowires. Red and blue balls represent different ions in the aqueous solution. The green rod and brown secondary structure represents the backbone MnO_2 and SnO_2, respectively.

Free-Standing $MnO_2/SnO_2/Al$ Ternary Thermite Membrane. Increasing attention has been drawn to search for superior and portable energetic materials to improve their implication in daily life, especially in microelectromechanical systems. Recently, our group prepared a novel thermite membrane composed of aluminum nanoparticles and MnO_2 nanowires.[31] Here, we employ this hierarchical nanostructure to prepare a novel MnO_2/SnO_2/n-Al ternary thermite membrane based on a bottom-up assembly method. Stoichiometric reactions between Al with MnO_2 and Al with SnO_2 can be illustrated in eqs 2 and 3. According to these chemical equations, the stoichiometric (st) fuel/oxidizer ratios are 0.414 and 0.239 for Al/MnO_2 and Al/SnO_2, respectively. The equivalence ratio of thermite membranes was chosen as 1.2, which corresponds with the commonly used equivalence ratio. The ratio of fuel to oxidizer (Ø) is defined as the fuel stoichiometric coefficient. Here, we assumed that predecessor stannic chloride pentahydrate was completely changed into SnO_2 for stoichiometric calculations. For pure MnO_2/Al binary composite, the fuel/oxidizer composites will be referred to as thermite C. For the MnO_2/SnO_2/n-Al ternary thermite composite, the fuel/oxidizer composites will be referred to as thermites C1, C2, and C3, which consist of different amounts of MnO_2 and SnO_2 as oxidizer. The amounts of MnO_2 in this ternary thermite change from 60.5% to 20%. More details about the composition of MnO_2/SnO_2/n-Al ternary thermite composites were summarized in Table S1 in the Supporting Information and a relevant report.[12]

$$4Al + 3MnO_2 \rightarrow 3Mn + 2Al_2O_3 \tag{2}$$

$$4Al + 3SnO_2 \rightarrow 3Sn + 2Al_2O_3 \tag{3}$$

The fabrication process of a free-standing ternary thermite membrane is illustrated in Figure S6 (see the Supporting Information for details). n-Al was dispersed via ultrasonic treatment in isopropanol forming a gray homogeneous suspension. In order to attain the membrane structure, MnO_2/SnO_2 hierarchical heterostructures were dispersed in $NH_4H_2PO_4$ aqueous solution rather than an organic solution. It is necessary to stress that the membrane structure cannot be assembled in pure organic solution. However, this membrane structure can be obtained with the help of an aqueous solution, which shows that the hydrogen bond plays an important role in this membrane.[32,33] $NH_4H_2PO_4$ was added to prevent the hydration in aqueous solution. Figure S7 shows that there is no obvious deterioration after dispersing in water. After a simple filtration method, membrane-like composites were obtained (Figure 6a), which can be easily separated from the filter paper without breakage. Notably, these free-standing thermite membranes were easily manufactured to a specific shape, which indicates its excellent processable property. Due to the high porosity of the membrane, n-Al can embed in these randomly oriented nanowires. The three dimensional schematic diagram in Figure 6a clearly shows that n-Al was perfectly

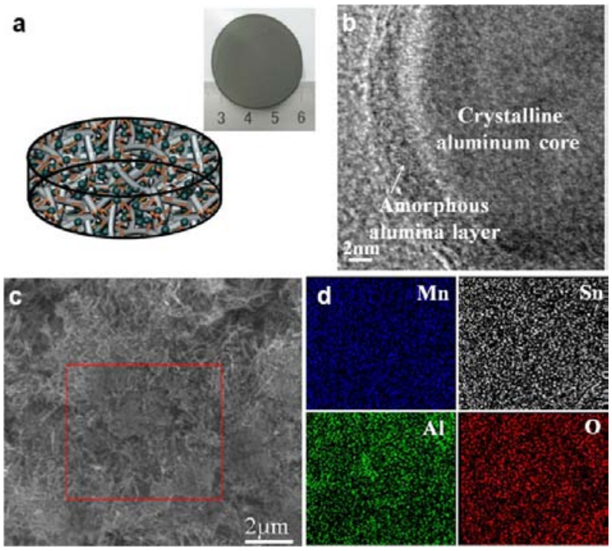

Figure 6. Characterization of MnO_2/SnO_2/n-Al ternary thermite membrane. (a) The three-dimensional schematic diagram of the as-obtained ternary thermite membrane. The inset optical image shows the free-standing ternary thermite membrane. (b) High-magnification TEM image of aluminum nanoparticles. (c) SEM microscopy image of MnO_2/SnO_2/n-Al ternary thermite membrane. (d) Elemental mapping of the selected area marked by a red line in c, indicating the homogeneous distribution of the reactants by this approach.

integrated into this assembly. The high-magnification TEM image (Figure 6b) reveals that there is an amorphous alumina passivation layer surrounding the aluminum core. Figure 6c shows SEM images of the as-obtained ternary thermite membrane. The energy dispersive X-ray (EDX) energy spectrum in Figure 6d undoubtedly shows that the good mixing of reactants was achieved in this membrane. It is logical to assume that this assembly method not only maximally decreases diffusion distances between the reactants but also effectively decreases the oxidation of aluminum.[16,31]

There are many factors, such as different types of reactants and surface modification, influencing the thermite kinetic constant. The different proportions of oxidizer composites were shown in Figure 7a. To investigate the reaction kinetics and ignition characteristics of the MnO_2/SnO_2/n-Al ternary thermite membrane, Differential Scanning Calorimetry (DSC) was carried out with a NETZSCH STA 449F3 device under various heating rates. Figure 7b−e show the DSC curves of different samples under different heating rates. For MnO_2/n-Al binary nanothermite composites (Figure 7b), the first exotherm of about 600 °C curves ascribes to the thermite reaction between the MnO_2 nanowires and n-Al. As shown in Figure 7e, it is obvious to see that there are no exotherms before the melting of Al (660 °C). That is to say, the introduction of SnO_2 has a great influence on the thermite reaction. The activation energy of different samples was determined to evaluate the corresponding reaction kinetics. The activation energy E_a (kJ/mol) is generally considered as the threshold energy to initiate the reaction. According to the Starink formula,[34] activation energy can be calculated by the following relation.

$$\ln\left\{\frac{T^{1.8}}{\beta}\right\} = (1.007 - 1.2 \times 10^{-5}E_a)\frac{E_a}{RT} + \text{Consta} \qquad (4)$$

where β is the heating rate (K/min), T is the peak temperature of the exothermic curve (K), and R is the universal gas constant. E_a can be refined from the slope of the linear graph of $\ln(T1.8/\beta)$ versus $1/T$ (illustration in Figure 7).[35,36] The results show the apparent activation energy of the MnO_2/n-Al binary mixture (sample C) change from 26.53 to 32.42 kJ/mol for the MnO_2/SnO_2/n-Al ternary mixture (sample C2). For sample C3, the thermite reaction does not occur before the melting of aluminum as the amount of SnO_2 increased to 42%. This result is consistent with the corresponding TG curves

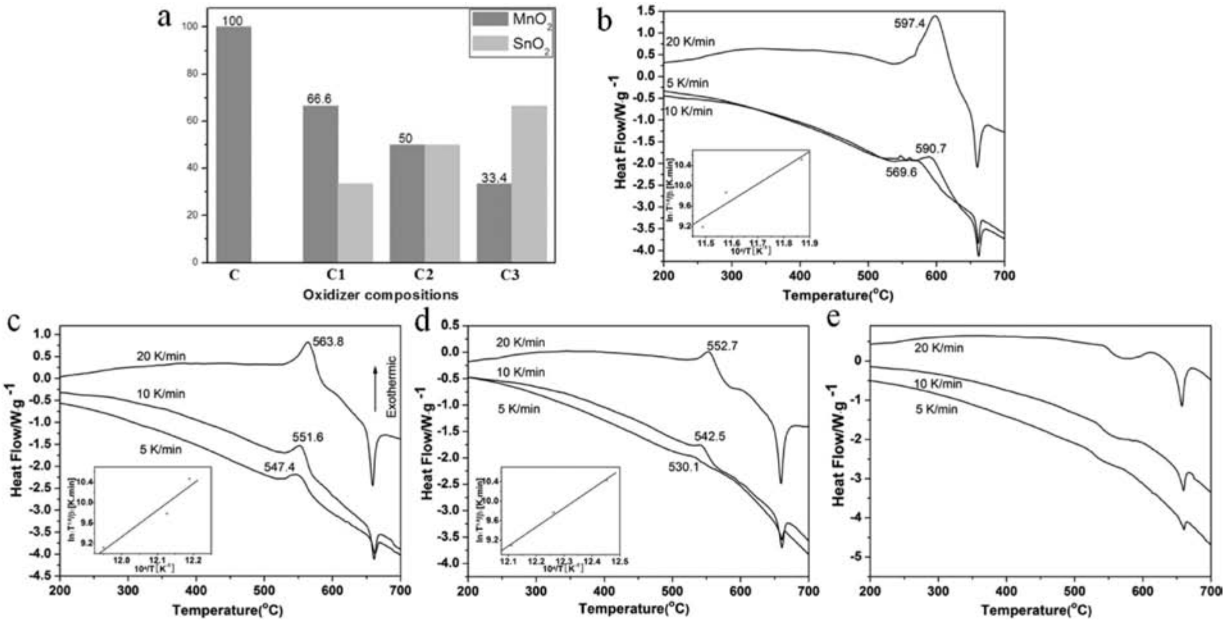

Figure 7. (a) Schematic diagram indicating different proportions of oxidizer composites. The mass fraction of MnO_2 in sample C1 is 66.6%. The mass fraction of MnO_2 in sample C2 is 50%. The mass fraction of MnO_2 in sample C3 is 33.4%. (b−d) DSC plot of exothermic reaction peaks at various heat rates in highly pure Ar atmosphere for the (a) MnO_2/Al composites, sample C1, (c) sample C2, (d) sample C3. The inset is the slope of the linear graph of $\ln(T^{1.8}/\beta)$ versus $1/T$.

(Figure S8). By comparing the different proportion of the thermite composites, the heat of reaction was qualitatively evaluated under the heating rate of 20 K min^{-1} (see Supporting Information, Figure S9). It is worth noting that the exothermic peak area gradually decreased with the increase of the content of SnO_2, which is consistent with previous results. However, the ignition temperature decreased from 563 to 552 °C as the amount of SnO_2 increased from 20 wt % to 31 wt %. It is logical to assume that the introduction of SnO_2 as an inert oxidizer changes the mechanism of the thermite reaction. However, the experimentally determined values of total heat of reaction are lower than the theoretical values and other thermite composites such as CuO/n-Al;[17] this is because the aluminum core was covered by an alumina passivation layer. The introduction of SnO_2 acts as an obstacle separating the interfacial contact between MnO_2 and n-Al so as to influence the thermite reaction mechanism. This novel ternary thermite mixture may find specific applications such as low heat and low onset temperature. Figure S10 shows the XRD pattern of the MnO_2/SnO_2/n-Al ternary mixture after reaction. The final reaction products are identified to be Al_2O_3, Mn_2O_3, and $MnSn_2$. The presence of tin and alumina shows that the thermite reacted as mentioned above (eqs 2 and 3). Manganic oxide may ascribe to the reoxidation of the formed manganese metal with oxygen during the thermite reaction.

■ CONCLUSIONS

MnO_2/SnO_2 hierarchical heterostructures with adjustable density of SnO_2 were synthesized via a surfactant-free hydrothermal method. The secondary growth SnO_2 on the surface of the MnO_2 backbone relies on the minimization of surface energy and interfacial lattice mismatch. This novel branched nanoheterostructure may have great potential application in, for example, battery materials. Moreover, we presented a bottom-up fabrication of n-Al and MnO_2/SnO_2 hierarchical heterostructures into a free-standing membrane with portable and tunable energetic performance. This assembly approach has the advantage of reducing diffusion distances as well as increasing particle contacts between the components. The introduction of SnO_2 may act as a barrier between the MnO_2 and n-Al, which provides a way to control the properties of energetic materials. Other characterizations, such as combustion velocity, are needed to further investigate the properties of this free-standing thermite membrane. This strategy provided here may be versatile to synthesize other highly energetic nanothermite composites. The present work enriches the preparation method of energetic materials but also expands a large amount of application in microelectromechanical systems.

■ ASSOCIATED CONTENT

Ⓢ Supporting Information

Additional SEM and TEM images, crystal structures illustration, XRD, TGA, and supplementary reaction tests. This material is available free of charge via the Internet at http://pubs.acs.org.

■ AUTHOR INFORMATION

Corresponding Author

*E-mail: wangxun@mail.tsinghua.edu.cn.

Notes

The authors declare no competing financial interest.

■ ACKNOWLEDGMENTS

This work was supported by NSFC (91127040, 21221062) and the State Key Project of Fundamental Research for Nanoscience and Nanotechnology (2011CB932402).

■ REFERENCES

(1) Milliron, D. J.; Hughes, S. M.; Cui, Y.; Manna, L.; Li, J. B.; Wang, L. W.; Alivisatos, A. P. *Nature* **2004**, *430*, 190−195.

(2) Lao, J. Y.; Wen, J. G.; Ren, Z. F. *Nano Lett.* **2002**, *2*, 1287−1291.

(3) Wu, Y.; Xiang, J.; Yang, C.; Lu, W.; Lieber, C. M. *Nature* **2004**, *430*, 61−65.

(4) Kuang, Q.; Jiang, Z. Y.; Xie, Z. X.; Lin, S. C.; Lin, Z. W.; Xie, S. Y.; Huang, R. B.; Zheng, L. S. *J. Am. Chem. Soc.* **2005**, *127*, 11777−11784.

(5) Wu, X.; Jiang, P.; Ding, Y.; Cai, W.; Xie, S. S.; Wang, Z. L. *Adv. Mater.* **2007**, *19*, 2319−2323.

(6) Agarwal, R. *Small* **2008**, *4*, 1872−1893.

(7) Chueh, Y. L.; Hsieh, C. H.; Chang, M. T.; Chou, L. J.; Lao, C. S.; Song, J. H.; Gan, J. Y.; Wang, Z. L. *Adv. Mater.* **2007**, *19*, 143−149.

(8) Rossi, C.; Zhang, K.; Esteve, D.; Alphonse, P.; Tailhades, P.; Vahlas, C. *J. Microelectromech. Syst.* **2007**, *16*, 919−931.

(9) Dreizin, E. L. *Prog. Energy Combust. Sci.* **2009**, *35*, 141−167.

(10) Siegert, B.; Comet, M.; Spitzer, D. *Nanoscale* **2011**, *3*, 3534−3544.

(11) Van der Heijden, A. E. D. M.; Creyghton, Y. L. M.; van de Peppel, R. J. E.; Abadjieva, E. *J. Phys. Chem. Solids.* **2010**, *71*, 59−63.

(12) Prentice, D.; Pantoya, M. L.; Clapsaddle, B. J. *J. Phys. Chem. B* **2005**, *109*, 20180−20185.

(13) Clapsaddle, B. J.; Sprehn, D. W.; Gash, A. E.; Satcher, J. H.; Simpson, R. L. *J. Non-Cryst. Solids.* **2004**, *350*, 173−181.

(14) Tillotson, T. M.; Gash, A. E.; Simpson, R. L.; Hrubesh, L. W.; Satcher, J. H.; Poco, J. F. *J. Non-Cryst. Solids.* **2001**, *285*, 338−345.

(15) Kim, S. H.; Zachariah, M. R. *Adv. Mater.* **2004**, *16*, 1821−1825.

(16) Zhang., K.; Rossi, C.; Rodriguez., G. A. A.; Tenailleau, C.; Alphonse, P. *Appl. Phys. Lett.* **2007**, *91*, 113117.

(17) Severac, F.; Alphonse, P.; Esteve, A.; Bancaud, A.; Rossi, C. *Adv. Funct. Mater.* **2012**, *22*, 323−329.

(18) Prakash, A.; McCormick, A. V.; Zachariah, M. R. *Nano Lett.* **2005**, *5*, 1357−1360.

(19) Armstrong, R. W.; Baschung, B.; Booth, D. W.; Samirant, M. *Nano Lett.* **2003**, *3*, 253−255.

(20) Niu, M.; Huang, F.; Cui, L.; Huang, P.; Yu, Y.; Wang, Y. *ACS Nano* **2010**, *4*, 681−688.

(21) Zhou, W.; Cheng, C.; Liu, J.; Tay, Y. Y.; Jiang, J.; Jia, X.; Zhang, J.; Gong, H.; Hng, H. H.; Yu, T.; Fan, H. J. *Adv. Funct. Mater.* **2011**, *21*, 2439−2445.

(22) Zhang, D. F.; Sun, L. D.; Jia, C. J.; Yan, Z. G.; You, L. P.; Yan, C. H. *J. Am. Chem. Soc.* **2005**, *127*, 13492−13493.

(23) Liang, H. W.; Zhang, W. J.; Ma, Y. N.; Cao, X.; Guan, Q. F.; Xu, W. P.; Yu, S. H. *ACS Nano* **2011**, *5*, 8148−8161.

(24) Zhou, W.; Tay, Y. Y.; Jia, X.; Wai, D. Y. Y.; Jiang, J.; Hoon, H. H.; Yu, T. *Nanoscale* **2012**, *4*, 4459−4463.

(25) Wang, X.; Li, Y. D. *J. Am. Chem. Soc.* **2002**, *124*, 2880−2881.

(26) Zhang, D. F.; Sun, L. D.; Yin, J. L.; Yan, C. H. *Adv. Mater.* **2003**, *15*, 1022−1025.

(27) Niu, M.; Cheng, Y.; Wang, Y.; Cui, L.; Bao, F.; Zhou, L. *Cryst. Growth Des.* **2008**, *8*, 1727−1729.

(28) Kang, J.; Kuang, Q.; Xie, Z. X.; Zheng, L. S. *J. Phys. Chem. C.* **2011**, *115*, 7874−7879.

(29) Zhang, Y. Q.; Sun, L. D.; Feng, W.; Wu, H. S.; Yan, C. H. *Nanoscale* **2012**, *4*, 5092−5097.

(30) Wang, Y.; Xu, J.; Wu, H.; Xu, M.; Peng, Z.; Zheng, G. *J. Math. Chem.* **2012**, *22*, 21923−21927.

(31) Yang, Y.; Wang, P. P.; Zhang, Z. C.; Liu, H. L.; Zhang, J. C.; Zhuang, J.; Wang, X. *Sci. Rep.* **2013**, *3*, 1694.

(32) Liu, J. W.; Liang, H. W.; Yu, S. H. *Chem. Rev.* **2012**, *112*, 4770−4799.

(33) Long, Y.; Hui, J. F.; Wang, P. P.; Xiang, G. L.; Xu, B.; Hu, S.; Zhu, W. C.; Lü, X. Q.; Zhuang, J.; Wang, X. *Sci. Rep.* **2012**, *2*, 612–618.
(34) Starink, M. J. *Thermochim. Acta* **2003**, *404*, 163–176.
(35) Cheng, J. L.; Hng, H. H.; Lee, Y. W.; Du, S. W.; Thadhani, N. N. *Combust. Flame* **2010**, *157*, 2241–2249.
(36) Fan, R. H.; Lu, H. L.; Sun, K. N.; Wang, W. X.; Yi, X. B. *Thermochim. Acta* **2006**, *440*, 129–131.